The Astrophysical Journal, 835:207 (9pp), 2017 February 1 doi:10.3847/1538-4357/835/2/207

Giant Lyα Nebulae in the Illustris Simulation

Max Gronke[1] and Simeon Bird[2]
[1] Institute of Theoretical Astrophysics, University of Oslo, Postboks 1029 Blindern, NO-0315 Oslo, Norway; maxbg@astro.uio.no
[2] Department of Physics and Astronomy, Johns Hopkins University, 3400 N. Charles St., Baltimore, MD 21218, USA
Received 2016 May 10; revised 2016 November 1; accepted 2016 December 16; published 2017 January 31

Abstract

Several "giant" Lyα nebulae with an extent $\gtrsim$300 kpc and observed Lyα luminosity of $\gtrsim 10^{44}$ erg s^{-1} cm^{-2} arcsec^{-2} have recently been detected, and it has been speculated that their presence hints at a substantial cold gas reservoir in small cool clumps not resolved in modern hydrodynamical simulations. We use the `Illustris` simulation to predict the Lyα emission emerging from large halos ($M > 10^{11.5}\,M_{\odot}$) at $z \sim 2$ and thus test this model. We consider both active galactic nucleus (AGN) and star driven ionization, and compare the simulated surface brightness maps, profiles, and Lyα spectra to a model where most gas is clumped below the simulation resolution scale. We find that with `Illustris`, no additional clumping is necessary to explain the extents, luminosities, and surface brightness profiles of the "giant Lyα nebulae" observed. Furthermore, the maximal extents of the objects show a wide spread for a given luminosity and do not correlate significantly with any halo properties. We also show how the detected size depends strongly on the employed surface brightness cutoff, and predict that further examples of such objects will be found in the near future.

Key words: galaxies: high-redshift – intergalactic medium – line: formation – quasars: general – radiative transfer – scattering

1. Introduction

The medium immediately surrounding galaxies—often dubbed the circumgalactic medium—provides a gas reservoir for star formation and as such is crucial for the study of galaxy formation and evolution. Extended faint Lyα emission originating from these regions directly probes this gas, uniquely so at higher redshifts where the observation of other emission lines is challenging (for reviews see, e.g., Barnes et al. 2014; Dijkstra 2014; Hayes 2015). These "Lyα nebulae" are often dubbed "Lyα blobs" (LABs), or when fainter and surrounding a galaxy also called "Lyα halos" (LAHs). While only a few LABs have been found so far (Fynbo et al. 1999; Steidel et al. 2000; Matsuda et al. 2011; Ao et al. 2015), it has been shown that LAHs surround Lyman-break or "drop-out" galaxies (LBGs), galaxies selected through their Lyα emission (Lyα emitters or LAEs), as well as Hα selected galaxies (recently shown by Matthee et al. 2016), leading to the conjecture that most (if not all) star-forming galaxies are associated with a LAH. Due to their very low surface-brightness (SB) profiles, a stacking technique is often used in order to study the properties of LAHs. Steidel et al. (2010) stacked a sample of 92 LBGs at $z \sim 2.65$ to reach SB limits of $\sim 10^{19}$ erg s^{-1} cm^{-2} arcsec^{-2} and found the LAHs extend out to $\sim$80 kpc with a exponential scale length of $r_{\alpha} \approx$ 20–30 kpc, which is a factor of a few larger than the scale length of the continuum emission. This result is consistent with the more recent finding of Matsuda et al. (2012), who used a set of 2128 LAEs and 24 LBGs at $z \sim 3.1$ to find scale lengths of $r_{\alpha} \sim$ 10–30 kpc and $r_{\alpha} \sim$ 20 kpc, respectively. Other studies (Rauch et al. 2008; Momose et al. 2014) support this picture but suggest a smaller LAH for LAEs as opposed to LBGs. This could however be an environmental effect if LBGs reside in higher-density environments (Matsuda et al. 2012). Furthermore, ultradeep MUSE observations recently revealed the LAHs surrounding 21 individual galaxies (Wisotzki et al. 2016). Without the need of stacking their SB profiles, they confirmed that the scale of the Lyα emitting region is several times larger than the scale of the continuum emission.

While the Lyα nebulae surrounding "normal" galaxies extend approximately tens of kiloparsecs and are relatively faint $L_{\alpha} \sim 10^{42}$ erg s^{-1}, LAHs around a rare $z \gtrsim 2$ population of galaxies sometimes dubbed "high redshift radio galaxies" (which are associated with one or multiple quasars) have extensions up to hundreds of kiloparsecs and luminosities of $L_{\alpha} \sim 10^{44}$ erg s^{-1} (Reuland et al. 2003; Villar-Martín et al. 2007; Trainor & Steidel 2012; Hennawi et al. 2015; Martin et al. 2015; Borisova et al. 2016). Cantalupo et al. (2014) detected the most massive of these nebulae (sometimes called the "slug nebula"), measuring a maximum extent of $\sim$450 kpc and $L_{\alpha} \sim 10^{45}$ erg s^{-1} ($L_{\alpha} \sim 2 \times 10^{44}$ erg s^{-1} excluding the emission directly from the quasar).

Although the existence of LABs, LAHs, and giant LAHs is observationally well-established, and some aspects are theoretically understood (e.g., their existence implies a fairly large hydrogen mass around dark-matter halos, Matsuda et al. 2012), some key questions remain unanswered. One that is debated in the literature is the energy source of these bright and extended Lyα nebulae. Generally, two possibilities are discussed: (i) Lyα production in the central region and subsequent scattering in the surrounding gas leading to the observed halo (e.g., Laursen & Sommer-Larsen 2007; Dijkstra & Kramer 2012), or (ii) in situ Lyα production in an extended region. The latter would be possible via, e.g., cooling luminosity of gas falling into the potential well of the galaxy (e.g., Haiman et al. 2000; Dijkstra & Loeb 2009). Alternatively, ionizing photons escaping from the central region or originating from nearby galaxies could lead to recombination events in the surrounding medium (e.g., Haiman & Rees 2001; Furlanetto et al. 2005; Mas-Ribas & Dijkstra 2016).

In particular, the discovery of giant LAHs poses the question of how Lyα emission can be located so far from an ionizing source. Cantalupo et al. (2014) carried out radiative transfer simulations on a zoom-in hydrodynamical simulation and

concluded that their model could not explain a Lyα object having this SB level and extent. Instead, they proposed that hydrodynamical simulations miss a substantial fraction of cold, dense clumps that will boost the Lyα luminosity. Specifically, they calculate the required clumping factor $C \equiv \langle n_e^2 \rangle / \langle n_e \rangle^2$ (where n_e is the electron number density) to be between 20 and 1000 on scales below a few kiloparsecs. In this work we want to revisit this question using the more modern cosmological hydrodynamical `Illustris` simulation (Vogelsberger et al. 2014; Nelson et al. 2015), which features a fully realized and well-tested model for galaxy formation, tuned to produce a realistic galaxy population at $z \sim 0$. This model includes efficient supernova feedback, metal cooling, and, importantly for studying the gas around quasars, a recipe for active galactic nucleus (AGN) feedback. Using this publicly available data allows us to study a statistically relevant ensemble of halos instead of focusing on individual objects.

The study is structured as follows. In Section 2 we lay out our model and numerical methods. We present our results in Section 3, and conclude in Section 4.

2. Methods

In this section, we first describe the hydrodynamical simulation used for our work (Section 2.1), then introduce our simple ionization models (Section 2.2) before explaining the Lyα radiative transfer simulation employed (Section 2.3).

2.1. The Hydrodynamical Simulation

The `Illustris` simulation (Vogelsberger et al. 2014) is a hydrodynamical cosmological simulation (simulation box side length of 106.5 cMpc) performed using the moving mesh code `AREPO` (Springel 2010). It includes gas cooling, and photo-ionization from a uniform ultra-violet background. Subgrid models are included for black holes and black hole feedback, stochastic star formation (with a density threshold of 0.13 cm^{-3} above which an ad hoc equation of state is imposed), stellar evolution, and stellar feedback, tuned to reproduce the Galaxy stellar mass function at $z = 0$. Note that molecular cooling is not included, and so the simulation does not accurately follow the temperature of gas with $T < 10^4$ K. In particular, we made use of the "Illustris-1" simulation which possesses a baryon (dark matter) particle mass of $12.6 \times 10^5\, M_\odot$ ($62.6 \times 10^5\, M_\odot$) and a resulting gravitational softening length of $\sim$700 pc (1.4 kpc). For the extraction of the data we made use of the excellent public interface provided by the `Illustris` team (Nelson et al. 2015), which allowed us to post-process individual cutout halos.

Inspired by the observations of Cantalupo et al. (2014), we selected a halo with total mass $M \sim 10^{12.5}\, M_\odot\, h^{-1}$ at $z \sim 2$. This halo possesses an active, central black hole with a mass inflow rate of $\dot{M}_{\rm BH} \sim 1.23\, M_\odot\ \mathrm{yr}^{-1}$, a initial neutral fraction of $\sim$26% and a cold ($T < 10^5\, K$) gas fraction of $\sim$30%. The total gas mass of this halo—as given by the simulation output—is $\sim 4.5 \times 10^{11}\, M_\odot\, h^{-1}$. The relevant quantities (per particle) for our work are: the cell volume $V_{\rm cell}$, the neutral hydrogen number density $n_{\rm H\,I}$, the ionized hydrogen number density $n_{\rm H\,II}$, the electron density n_e, the gas velocity $\boldsymbol{v}$, the star formation rate SFR, the metallicity Z, and the temperature T. We compute T as

$$T = \frac{2u\mu}{3k_{\rm B}}, \tag{1}$$

where u is the internal energy, μ the mean molecular weight of the gas, and $k_{\rm B}$ the Boltzmann constant. Dust plays a crucial role in Lyα radiative transfer and dust reddening is expected to be important in these massive halos. We follow Laursen et al. (2009) and calculate an effective number density of dust atoms as

$$n_d = (n_{\rm H\,I} + f_{\rm ion}\, n_{\rm H\,II}) \frac{Z}{Z_\odot} \tag{2}$$

which defines a dust optical depth through $\tau_d = n_d \sigma_d d$, where σ_d is the dust optical depth and d the path length considered. For the former, we use the value of the Small Magellanic Cloud $\sigma_{{\rm Ly}\alpha,{\rm SMC}} \approx 1.58 \times 10^{-21}\,\mathrm{cm}^2$ Pei (1992) and take the dust-to-gas ratio in an ionized region to be characterized by $f_{\rm ion} = 0.01$ (see Section 2.2.1 in Laursen et al. 2009 for a detailed discussion of why this choice is a good approximation). The effect of dust is a major source of uncertainty in our work; we discuss the effect of this uncertainty in Sections 3.2 and 3.4. In order to demonstrate its impact, we also show some radiative transfer results excluding dust reddening.

Self-shielding of gas from the metagalactic UV background is included in `Illustris` using the prescription of Rahmati et al. (2013a). This includes the neutral fraction in the (subgrid) star-forming gas, which is roughly unity, neglecting the local radiation field of the forming stars.

2.2. The Model

In addition to the halo (as described in the previous section), we consider two possibilities for the radiation field:

1. *AGN ionization.* In this scenario, we fully ionize all the cells falling within a spherical region around the central black hole with radius $r_{\rm ion}$. This clearly is a simplification of the true ionization mechanism by quasars as we neglect radiative transfer effects from different density structures as well as the likely existence of conical jets. However, in this work we are content with a first order approximation, as Cantalupo et al. (2014) demonstrated that it was not possible to resolve the discrepancy between the observations and simulations without extra subgrid clumping even in the extreme cases when *all* the hydrogen is ionized or neutral. Quasars can potentially ionize a region up to several megaparsecs (Cen & Haiman 2000). However, we choose a relatively small value for $r_{\rm ion}$ in Section 3.2 in order to (i) show the radiative transfer effect in the outer region (i.e., to be much smaller than the total extent of the LAH), and (ii) still be large enough so that a small change in $r_{\rm ion}$ does not lead to a significant change in the intrinsic luminosity (Section 3.1). As a fiducial value we pick $r_{\rm ion} = 20$ kpc.
2. *Ionization from stars.* Here, we ionize all the star-forming cells by subtracting

$$\Delta X_{\rm H\,I} = \frac{Q_{\rm ion} m_{\rm ion}}{n_{\rm H\,I}^2 \alpha_{\rm B}(T) V_{\rm cell}} \tag{3}$$

from the cells' neutral hydrogen fraction, while ensuring $X_{\rm H\,I} \geqslant 0$. In the above equation, $\alpha_{\rm B}$ is the case-B recombination coefficient (see below) and

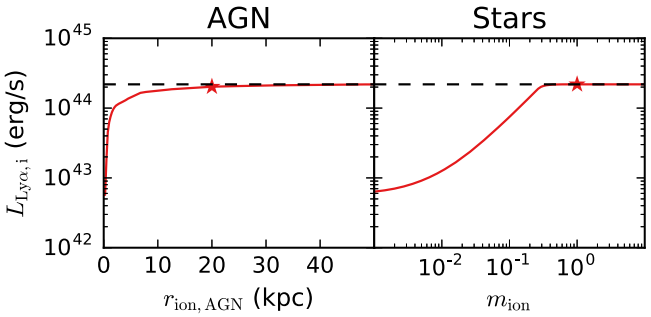

Figure 1. Intrinsic Lyα luminosities for the two models. The black-dashed line denotes the intrinsic luminosity reached if the entire grid is fully ionized, and the red star symbols illustrate the choice of our fiducial models. It is clear that in each model reaching the maximal possible luminosity with the gas as given by the hydrodynamical simulation output is possible with either moderate ionization activity from either the star forming regions or the black hole.

$Q_{\mathrm{ion}} = 2 \times 10^{53} \frac{\mathrm{SFR}}{1\,M_{\odot}\,\mathrm{yr}}$ for a range of different stellar models (Rahmati et al. 2013b). Here, the free parameter m_{ion} can be interpreted as the number of (fully ionized) Strömgren spheres (volume $Q_{\mathrm{ion}}/(n_{\mathrm{H\,I}}^2 \alpha_{\mathrm{B}})$) placed in a neutral cell. This means for a cell with $X_{\mathrm{H\,I}} = 1$ if there is one star (cluster) per cell, the "sub-grid" escape fraction of ionizing photons is unity and if the ionized region does not overlap with the boundary then $m_{\mathrm{ion}} \sim 1$. In reality it is likely that the escape fraction is less than unity, and that nearby cells are also affected by ionizing photons. Furthermore, we expect several massive stars within each cell, given that the typical lifetime of a massive star is 5–10 Myr. However, given the uncertainty in calculating these effects, and the fact that, as shown in Figure 1, the Lyα luminosity saturates at $m_{\mathrm{ion}} \approx 0.2$, $m_{\mathrm{ion}} = 1$ appears to be a reasonable fiducial value and we adopt it for the rest of the paper.

These model parameters are summarized in Table 1. The total amount of gas within the simulation is conserved in both the scenarios considered. We assume that the ionizing radiation fields are sufficiently intense that the gas will be highly ionized (Hennawi & Prochaska 2013). In fact, if we allow the hydrogen neutral fraction in the *maximally* ionized regions we reach a minimum value of $X_{\mathrm{H\,I,\,min}} = 0$. As the emissivity $\propto (1 - X_{\mathrm{H\,I}})^2$ a slightly larger value of $X_{\mathrm{H\,I}}$ will not have a strong effect on the SB values (however, it can affect the Lyα radiative transfer, see Section 3.3).

Given the number density of ionized hydrogen $n_{\mathrm{H\,II}}$, the electron number density n_e and a temperature T per cell, we compute the total Lyα luminosity assuming solely "case-B" recombination[3]

$$L_{\alpha,\mathrm{i}} = \sum_{\mathrm{cells}} n_{\mathrm{H\,II}} n_e N_{\alpha}(T) \alpha_B(T) V_{\mathrm{cell}}, \quad (4)$$

where $\alpha_B(T)$ is the "case-B" recombination coefficient from the fitting formulae by Hui & Gnedin (1997), and $N_{\alpha}(T)$ is the average number of Lyα photons produced per "case-B" recombination event. For $N_{\alpha}(T)$ we adopt the fit provided by Cantalupo et al. (2008). As Lyα is produced mainly in high-density environments, the contribution of "case-A" recombination can be safely neglected (Gould & Weinberg 1996). Lyα cooling radiation is highly sensitive to the temperature of the cold gas and no consensus has been reached on its contribution (Furlanetto et al. 2005; Faucher-Giguère et al. 2010; Goerdt et al. 2010; Rosdahl & Blaizot 2011; Cen & Zheng 2013). In order to assess its impact a fully coupled radiation-hydrodynamical simulation is preferable (as, e.g., in Rosdahl & Blaizot 2011), which can in principle model the temperature state of the ISM. We do not address the impact of cooling radiation in this work, and, thus neglect its contribution. Both choices only reduce the final luminosity.

[3] "Case-B" recombination denotes the recombination in a medium which is optically thick to ionizing photons. This leads to the immediate re-absorption of an emitted ionizing photon (see, e.g., Osterbrock 1989; Dijkstra 2014, for details).

Table 1
Overview of the Model Parameters

Model	Parameter	Description	Fiducial Value
AGN	r_{ion}	Radius of ionized region around AGN	20 kpc
Stars	m_{ion}	Cell volume ionized in units of Strömgren spheres (Equation (3))	1

2.3. Radiative Transfer Calculations

Prior to carrying out the full Lyα radiative transfer calculation we interpolate the individual halo from the hydrodynamical simulation to a Cartesian grid with $512 \times 528 \times 449$ cells (corresponding to a uniform side-length of each cell of $\sim$1.63 kpc), while keeping constant the number of hydrogen atoms, the number of dust grains, the number of clouds placed on the grid and the total Lyα luminosity. For the conversion from the moving-mesh structure to a Cartesian grid (used by `AREPO` (Springel 2010) and the radiative transfer calculations, respectively), we used `splash` (Price 2012) with a smoothing length[4] of $l_{\mathrm{smooth}} = 4 \times V_{\mathrm{cell}}^{1/3}$ which corresponds to $\sim$58 neighboring particles. We repeated our analysis for one model using half the number of cells per dimension and find the results to be unaffected. After the conversion, the number of clouds in each cell is rounded to the nearest integer, redistributing the cutoff material self-consistently and the clouds are placed randomly within each cell.

The Lyα radiative transfer calculations are carried out using the Monte-Carlo radiative transfer (MCRT) code `tlac` (Gronke & Dijkstra 2014). General descriptions of MCRT are given in Dijkstra (2014) or Laursen (2010). The specific settings of `tlac` we employed are identical to Gronke & Dijkstra (2016) and we merely summarize them here. We ran each MCRT simulation using at least 2×10^6 photon packages, which we placed randomly on the gas density grid. The probability to position a photon package in a certain cell (i.e., the weight of this cell) was proportional to the cell's intrinsic luminosity. We draw the intrinsic frequency of a photon package from a Voigt profile, the convolution of the natural (Lorentzian) line profile, and the thermal (Gaussian) profile of the emitting atoms of the initial cell. The process of image making with `tlac` has not been published previously and we describe the method below.

Producing SB maps with MCRT can be challenging as the number of individual photon packages escaping in a specific direction is essentially zero. Therefore, we use a commonly used technique sometimes called the "peeling" algorithm

[4] We used the default M_4 cubic B-spline kernel.

(Yusef-Zadeh et al. 1984; Zheng & Miralda-Éscude 2002; Laursen 2010). In every Nth scatter event (including the emission step), the optical depth, $\tau_{\rm obs}(\nu_v)$, in the direction $\boldsymbol{k}_{\rm obs}$ is recorded. Here, ν_v is the frequency that the photon would have had if it had flown in the direction $\boldsymbol{k}_{\rm obs}$. This assigns a weight[5] to this scattering event that is the escape probability along $\boldsymbol{k}_{\rm obs}$ given by:

$$w = \frac{N}{2} e^{-\tau_{\rm obs}(\nu_v)}, \tag{5}$$

where N is the frequency of recorded scattering events discussed above. The SB for pixel j can then be calculated using

$$\mathrm{SB}_j = \frac{L_{\alpha,\mathrm{i}} S_j}{D_L^2(z)\,\Omega_{\mathrm{pix},j} N_{\rm phot}}, \tag{6}$$

where $N_{\rm phot}$ is the total number of photon packages emitted, $D_L(z)$ is the luminosity distance corresponding to redshift z, $\Omega_{\mathrm{pix},j}$ is the solid angle of pixel j and $S_j = \sum_j w$ is the sum of weights of the photons falling withing this pixel. Naturally, if calculating an observed spectrum, the weights w have to be taken into account as well, and each frequency bin consists of the sum of the photons' weights.

3. Results

In this section, we present first results from our "fiducial" halo (Sections 3.1–3.3) and put them into a wider context in Section 3.4. Specifically, we carry out full Lyα radiative transfer simulations for the former part—from which we show SB maps and profiles (Section 3.1) and Lyα spectra (Section 3.3). In the latter part, we compare the full distribution of LAHs found in the `Illustris` simulations to observations.

3.1. Intrinsic Lyα Luminosities

Figure 1 shows the intrinsic Lyα luminosity for the models presented in Section 2.2. In each of the panels, the black dashed line shows the value if the whole grid (i.e., the selected halo) were ionized, and the star symbol marks the fiducial values in each model. The two leftmost panels show that quite moderate ionization activity from either the star-forming regions or the AGN is able to saturate the luminosity allowed by the gas distribution, as given by the hydrodynamical simulation output. Also noticeable is the proximity of the computed Lyα luminosity ($L_{\alpha,\mathrm{i,max}} \sim 2 \times 10^{44}\,\mathrm{erg\,s^{-1}}$) and the observed value by Cantalupo et al. (2014) ($\sim 2 \times 10^{44}\,\mathrm{erg\,s^{-1}}$ excluding the emission directly from the quasar). The luminosity saturates because the densest regions are already ionized. For the "stars" model this occurs at $m_{\rm ion} \gtrsim 0.3$ and for the "AGN" model for $r_{\rm ion} \gtrsim 15$ kpc. For even greater radii the gas density drops off —and so does the increase in luminosity.

3.2. Surface Brightness

Figure 2 shows the surface brightness maps for our two models (see Section 2.2) and one specific observing direction computed as given by Equation (6). In order to resolve the SB maps sufficiently we ran the radiative transfer calculations with at least 2 million photons, each leading to a minimum of 300,000 recorded events for each of the four observers' directions. In the Appendix we show the intrinsic SB maps, i.e., without radiative transfer, for comparison.

Figure 2 shows very similar topography in both the AGN- and star-ionization models. The stars produce slightly more prominent features in the outskirts of the halo. Both cases have an maximal extent of $\sim$350 kpc for this particular sightline, a central SB of $\sim 10^{-15}\,\mathrm{erg\,s^{-1}\,cm^{-2}\,arcsec^{-2}}$, which falls to $\sim 10^{-18}\,\mathrm{erg\,s^{-1}\,cm^{-2}\,arcsec^{-2}}$ in the outer regions. Overall, the size of this simulated nebula falls $\sim$100 kpc short of the projected maximum extent measured by Cantalupo et al. (2014). However, if restricted to SB contours $\gtrsim 10^{-18}\,\mathrm{erg\,s^{-1}\,cm^{-2}\,arcsec^{-2}}$ then the measurement is reduced by $\sim$20% (Cantalupo et al. 2014), which brings the two measures very close to each other. Figure 2 also shows the "AGN" case but without the inclusion of dust (rightmost panel). Here, one can notice that the morphology and SB levels are different, that is, in the case without dust the halo is extended and overall brighter.

Figure 3 shows a more quantitative comparison of the surface brightness between the two models. Here we display the SB profiles, as well as the intrinsic SB profiles, as a function of distance from the black hole, observed from the same direction as in Figure 2. The same features are visible, with the curves of the "stars" and "AGN" cases following each other closely. Note, however, that the SB in this case is an angular averaged value and thus dependent on the geometry of the halo. This leads to variations in the radial profile depending on the observer's direction. The black dashed line in Figure 3 denotes the "virial radius" R_{200c}, i.e., the radius at which the average density is 200 times the critical density at $z \sim 2$. In all cases the central SB values are significantly reduced compared to their intrinsic values, due to dust extinction (also see Laursen et al. 2009) and re-distribution of photons due to radiative transfer effects. However, in the outer parts of the halo the intrinsic and post-processed SB values approach each other.

In order to be able to distinguish between the effect of dust attenuation and systematic radial re-distribution of photons due to radiative transfer effects, we also show in Figure 3 the "AGN" case without any dust (green line). Radiative transfer reduces the SB values in the inner part of the halo, but increases them at larger radii. Thus, scattering increases the effective size of LAHs (as also found by Trebitsch et al. (2016), in their dust-free simulations). Note though that these re-distributed photons will also experience a relatively large dust optical depth, leading to lower SB values (as can be seen when comparing the two "AGN" curves in Figure 3). When considering, for example, the width of a halo with SB $>10^{-18}\,\mathrm{erg\,s^{-1}\,cm^{-2}\,arcsec^{-2}}$, these different effects would lead to uncertainties of a factor of $\sim$2. In particular, hydrogen scattering tends to increase the apparent size compared to the intrinsic emission, while dust absorption decreases it. This may be of importance when comparing to observations and will be discussed again in Section 3.4.

3.3. Lyα Spectra

Figure 4 shows spectra resulting from the full Lyα radiative transfer simulations. These spectra are taken from the same direction as the SB values from Section 3.2. The spectra are

[5] Note that although we consider the slightly differing redistribution functions for the scattering via the $2P_{1/2}$ and the $2P_{3/2}$ states for the full radiative transfer process, we assume a uniform angular probability density function for the potential scattering toward $\boldsymbol{k}_{\rm obs}$. However, due to the large number of photons that escaped without scattering ($\sim$35%) and thus do not possess any preferred direction, we do not expect that our results are affected by this.

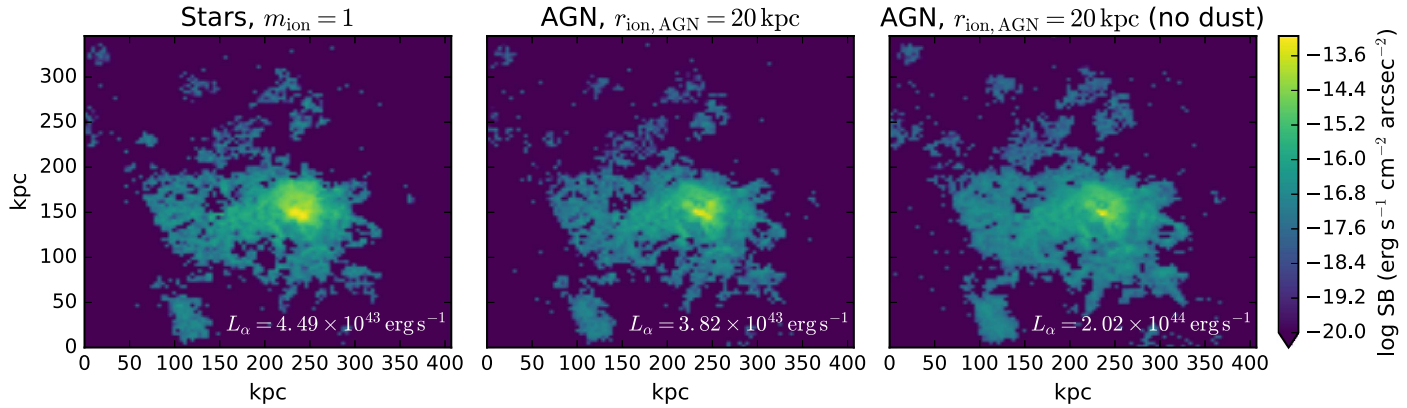

Figure 2. Surface brightness maps for the fiducial models (from left to right panel): star-driven ionization, AGN-driven ionization, and AGN-driven ionization without dust (see Section 2.2).

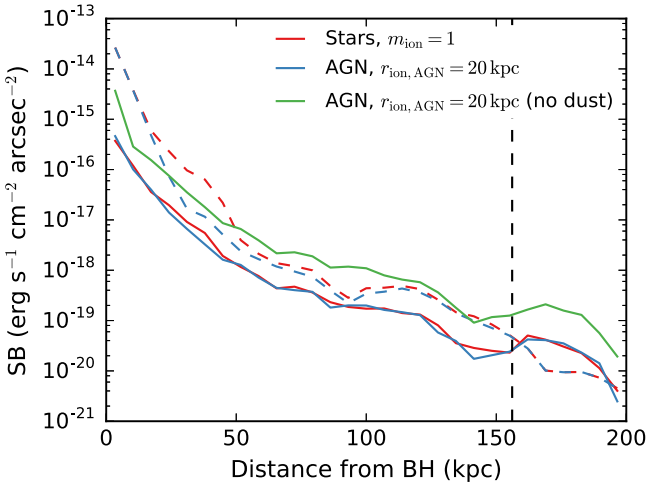

Figure 3. Radially binned surface brightness profile as a function of distance from the black hole for the fiducial models as "seen" by an observer directed in the same way as in Figure 2. The dashed and solid lines show the (intrinsic) surface brightness profile before and after the radiative transfer calculations, respectively. The vertical line denotes the virial radius of this halo (R_{200c}).

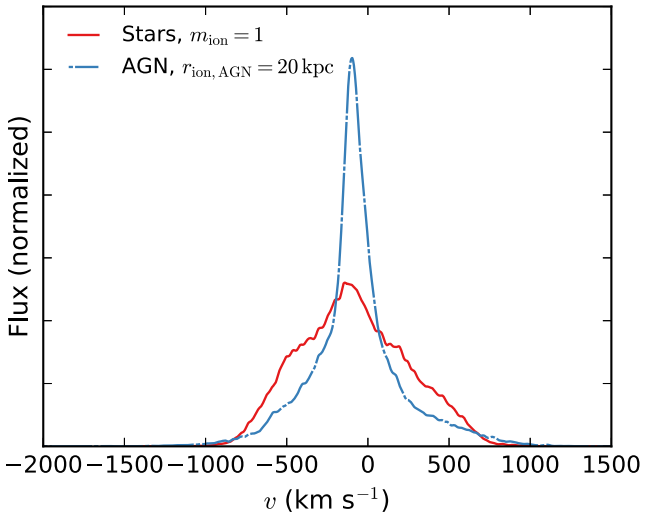

Figure 4. Lyα spectra taken from both our models in the direction used in Figure 3. Note that the shapes of the spectra depend strongly on our fiducial model parameters (see Section 3.3).

single peaked, showing the features expected from a low optical depth system. While the "AGN" case shows a peaked profile, the spectrum emerging from our "stars" model is more rounded and wider, with a slightly peaked feature at the line center.

One has to be cautious, however, when interpreting the Lyα spectra shown in Figure 4, as the applied resolution is not sufficient to capture the full Lyα radiative transfer dynamics (see, e.g., Verhamme et al. (2012), who showed that $\sim$pc resolution is necessary), and their shape heavily relies on the model parameters, such as the minimally allowed neutral fraction for ionized cells $X_{\rm H\,I,min}$. This value—which is zero for our fiducial models—strongly influences the emergent spectral shape. We tested this by increasing $X_{\rm H\,I,min}$ to the rather extreme value of 10^{-3} in the "AGN" case and obtained wide (peak separation of $\sim$1500 km s^{-1}) double peaked spectra instead. In addition, we find the spectral shape to be dependent on the observer's direction. In particular, the flux at line center is significantly lower (however, not so low as to form a double peaked profile) for other directions in which the optical depth between the observer and the emitting region is higher. This illustrates the difficulty of using ab initio hydrodynamical simulations to predict the outcome of Lyα spectra and their comparison with observations (see Section 4 for a discussion of this point).

3.4. Comparison to Observations

Cantalupo et al. (2014) observed a giant LAH with luminosity of $L_\alpha = (2.2 \pm 0.2) \times 10^{44}$ erg s^{-1} ($L_\alpha \approx 1.43 \times 10^{45}$ erg s^{-1} including the central quasar) and maximal projected extent of 460 kpc (SB $> 10^{-18}$ erg s^{-1} cm^{-2} arcsec^{-2}).[6] A similar—slightly smaller—object was observed by Hennawi et al. (2015), with a total Lyα luminosity of $L_\alpha \approx 2.1 \times 10^{44}$ erg s^{-1} and a maximum extent of 310 kpc. The $\sim 10^{12.5}\,M_\odot$ halo we selected from the `Illustris` simulation shows very similar intrinsic Lyα luminosities ($L_{{\rm i},\alpha} \sim 2 \times 10^{44}$ erg s^{-1}) and extents even without introducing additional clumping below the simulation resolution. In our fiducial models, the Lyα escape fraction was always $\sim$25%, leading to a slightly smaller Lyα luminosity than observed. However, as the escape fraction is given by small-scale radiative transfer physics, we see the obtained escape fraction as a lower limit to the real value. In particular, two points are rather uncertain. First, the conversion between metallicity and Lyα dust

[6] We acknowledge that it is difficult observationally to distinguish between quasar and nebula emission. Note, however, that the luminosity *including* the quasar can be seen as an upper limit to the nebular emission.

optical depth as given by Equation (2) is calibrated to local values and it is unclear how reliable it is when applied to $z \sim 2$ systems. Furthermore, if the dust is not spread uniformly (below the radiative transfer resolution scale), "dust-free channels" might enhance the Lyα escape fraction.

As already mentioned in Section 3.2, the non-unity escape fractions and radiative transfer effects will have an impact on the maximal extent of the LAH, too. In particular, for our "fiducial" halo presented previously we found that while the intrinsic maximum extent (for which SB $> 10^{-18}$ erg s^{-1} cm^{-2} arcsec^{-2}) is $\sim$250 kpc (for the AGN- and star-ionization cases), the post-processed maximum extent is $\sim$318 and $\sim$415 kpc with and without dust, respectively.[7] That Lyα scattering tends to increase the observed size of an object is frequently inferred for other objects; galaxies, for instance, show significantly larger LAHs compared to their UV counterparts (e.g., Hayes et al. 2014; Wisotzki et al. 2016). Other theoretical work seems to confirm this picture (e.g., Trebitsch et al. (2016), found that including radiative-transfer effects enlarges the LAH in their simulation by $\sim$10%). We therefore conclude that the re-distribution of photons in the outer regions tends to increase the maximum extent of the halo, and use as a conservative measure the intrinsic values in this section. We also note that uncertainties in the impact of Lyα radiative transfer persist, as the H I and dust structure on the smallest scales are unknown—which might alter our results.

3.4.1. Maximal Extents

In order to determine whether this halo is an exceptional case —without running the full Lyα radiative transfer simulations on several halos—we used the intrinsic Lyα luminosity as given by Equation (4) to compute "intrinsic surface brightness maps" from which we can measure the maximum projected extent. This approach is supported by the findings presented in Section 3.2, namely that radiative transfer effects and dust extinction dim the central brightest regions of the halo, but only moderately increase the outer regions. Since we are interested primarily in these regions when comparing the simulations to observed size measurements, we suspect using intrinsic luminosities will only moderately underestimate the maximal extents in our simulated halos. Specifically, we used 15 halos per $\log \Delta M/M_\odot = 0.5$ mass bin for the masses between $10^{11.5}\,M_\odot$ and $10^{13.5}\,M_\odot$ which we ionized according to our "ionization from stars" model[8] with $m_{\rm ion} = 1$. To mimic the observations, we then smooth the SB maps with a Gaussian kernel (FWHM = 1 arcsec) and then measure the maximal extent for pixels with SB$_i > 10^{-18}$ erg s^{-1} cm^{-2} arcsec^{-2}.

Figure 5 shows the result of this analysis as the maximal extent versus the intrinsic luminosities of the 45 halos. The points and error bars represent the 16th, 50th, and 84th percentiles of the distribution of extents created though 100 randomly drawn observer's directions, and the color coding denotes the mass of the halo. Note that the size of the error bars thus shows a substantial size-variation with viewing angle. In addition, we displayed the observations quoted above. These are not, however, the intrinsic values. $L_{\alpha,\rm i}$ for the observed nebula is probably a factor of a few larger, and SB$_{\rm i}$ should also

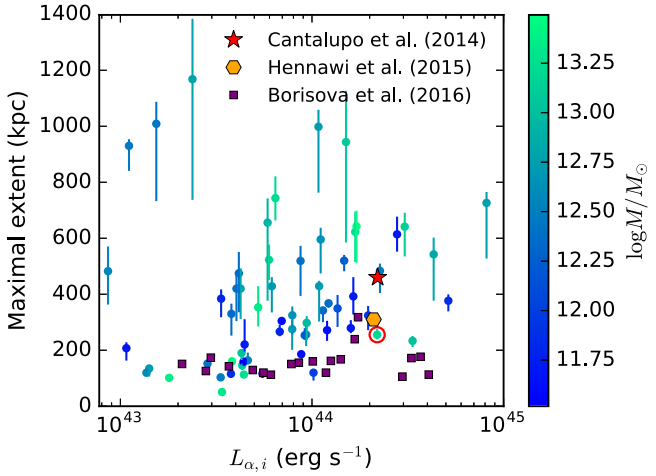

Figure 5. Maximal extent for halos in mass bins from $10^{11.5}\,M_\odot$ to $10^{13.5}\,M_\odot$ using a SB cutoff of 10^{-18} erg s^{-1} cm^{-2} arcsec^{-2} vs. intrinsic Lyα luminosity. The error bars denote the variance between various directions and the red circle highlights the "fiducial" halo shown in the previous figures. Also shown are the observations from Cantalupo et al. (2014), Hennawi et al. (2015), and Borisova et al. (2016), which implicitly assume $f_{\alpha,\rm esc} \sim 1$. See Section 3.4 for a detailed discussion.

be (slightly) increased. Nevertheless, Figure 5 illustrates that LAHs with similar extent & luminosity can be found in the `Illustris` simulation. Another interesting feature is that the extent does not seem to correlate with mass and/or $L_{\alpha,\rm i}$. We also checked the correlation of the extent versus various other halo properties (gas mass, gas metallicity, black hole mass) and found none of them to correlate significantly with the extent (all the Pearson as well as the Spearman correlation coefficients were within $[-0.3, 0.3]$). The reason for this is that the quantity "maximal projected extent" is primarily a geometrical measurement and, hence, highly dependent on the topology of the gas configuration.

3.4.2. Alternative Size Measurements

As an alternative to the "maximal extent" measure, we plot in Figures 6 and 7 the projected area covered by the LAHs, and the radius for which the radially averaged SB profile falls below SB$_{\rm cut}$, respectively. Again we used a cutoff of SB$_{\rm cut} = 10^{-18}$ erg s^{-1} cm^{-2} arcsec^{-2} and a FWHM of the convolved Gaussian kernel of 1 arcsec. It is noticeable that the correlation between area covered as well as the "crossing radius" and intrinsic Lyα luminosity is slightly better than between the maximal extent and $L_{\alpha,\rm i}$ shown in Figure 5 (Spearman coefficients of $\sim$0.65 and $\sim$0.72 versus $\sim$0.34). However, a significant scatter still persists. Figure 7 shows a comparison the objects from Cantalupo et al. (2014), Hennawi et al. (2015), and Borisova et al. (2016). The radial extent of the first two was estimated from Figure 12 of Battaia et al. (2016), and thus implicitly assumes a Lyα fraction of unity, as already discussed above for Figure 5.

3.4.3. Size Dependence on SB Cutoff

It initially appears puzzling that LAHs with this extent have not been detected previously, as is nicely illustrated in Figure 3 of Cantalupo et al. (2014). However, as noted in that work, one has to take into account that previous halos were measured with a surface cutoff of SB$_{\rm cut} = 3 \times 10^{-18}$ erg s^{-1} cm^{-2} arcsec^{-2}, whereas Cantalupo et al.

[7] These values are for the "AGN" case ($r_{\rm ion} = 20$ kpc) and the mean of four directions orthogonal to each other. A smoothing with FWHM = 1 arcsec has been applied.

[8] As shown in Section 3 the "AGN" and "star" cases are very similar and also an increase of $m_{\rm ion}$ above $\sim$0.3 does not alter $L_{\alpha,\rm i}$. Because not all (sub)halos possess black holes, however, we chose the "star" model for simplicity.

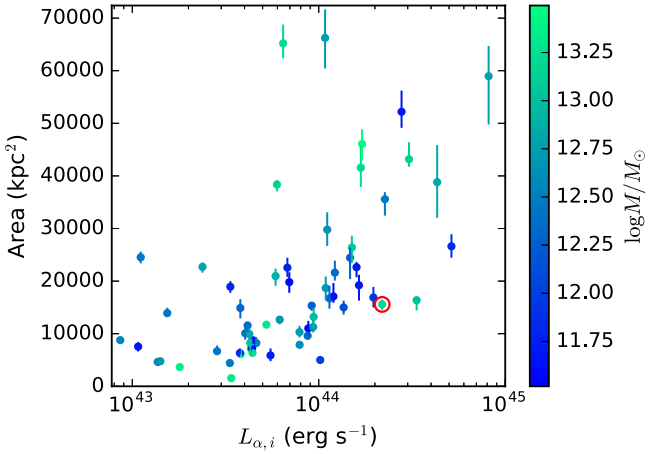

Figure 6. Projected area for halos in mass bins from $10^{11.5}\,M_\odot$ to $10^{13.5}\,M_\odot$ using a SB cutoff of 10^{-18} erg s^{-1} cm^{-2} arcsec^{-2} vs. intrinsic Lyα luminosity. The error bars denote the variance between 100 randomly drawn directions and the red circle marks the "fiducial" halo shown in Figures 1–3.

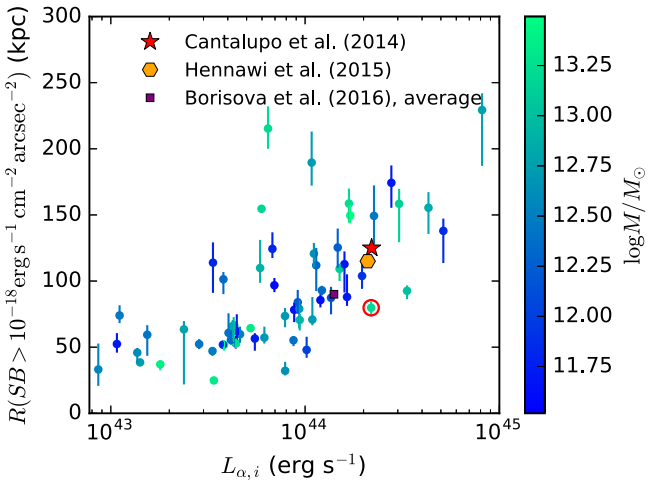

Figure 7. Lyα luminosity radius in which the SB (radially averaged) is $>10^{-18}$ erg s^{-1} cm^{-2} arcsec^{-2} vs. Lyα luminosity for halos in mass bins from $10^{11.5}\,M_\odot$ to $10^{13.5}\,M_\odot$ using a SB cutoff of 10^{-18} erg s^{-1} cm^{-2} arcsec^{-2} . As previously, the error bars denote the variance between 100 randomly drawn directions and the red circle highlights our "fiducial halo." Also shown are the observations from Cantalupo et al. (2014) and Hennawi et al. (2015) (estimated from Figure 12 of Battaia et al. 2016) as well as the average profile of Borisova et al. (2016) which implicitly assumes $f_{\alpha,\rm esc} \sim 1$ (see Section 3.4).

(2014) used $\mathrm{SB_{cut}} = 10^{-18}$ erg s^{-1} cm^{-2} arcsec^{-2} . That this difference matters is shown in Figure 8, where we plot how the maximal extent varies with chosen surface brightness cutoff $\mathrm{SB_{cut}}$. In particular, we show[9] the mean of the maximal extent using 10 random observer directions and normalized it to the mean of 100 random observer directions for $\mathrm{SB_{cut}} = 10^{-18}$ erg s^{-1} cm^{-2} arcsec^{-2} (as used in Figure 5). Figure 8 shows that the exact value of $\mathrm{SB_{cut}}$ can alter the measured projected extent dramatically and even a moderate change of a factor of three, as discussed above, can decrease the size by ∼50%. Interestingly, lowering $\mathrm{SB_{cut}}$ to 10^{-19} erg s^{-1} cm^{-2} arcsec^{-2} might more than double the size, but even fainter cutoffs do not increase the extent further.

While we were finalizing this work, two new studies appeared examining extended LAHs. Battaia et al. (2016)

[9] For illustration purposes we show only 15 randomly selected halos.

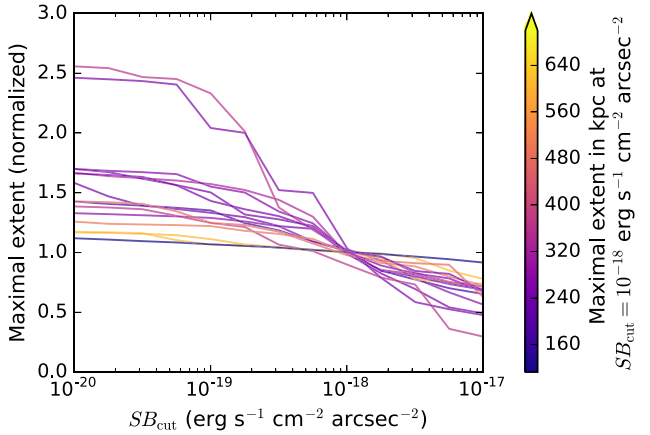

Figure 8. Maximal extent vs. the surface brightness cutoff $\mathrm{SB_{cut}}$. Each line represents one of 15 randomly selected halos for which we plot the mean (using 10 random observer directions) normalized to the value at $\mathrm{SB_{cut}} = 10^{-18}$ erg s^{-1} cm^{-2} arcsec^{-2} (for 100 random observer directions). The color coding denotes the value of normalization.

examined 15 quasars at $z \sim 2$ and found no extended nebulae. In contrast, Borisova et al. (2016) examined a sample of 17 radio-quiet quasars at $3 < z < 4$ and found a nebula with extent >100 kpc in every case examined (see also Herenz et al. (2015), who found in 4 out of 5 cases no extended nebula). There thus seems at present some disagreement as to the abundance of these objects. Whether this is due to the differing samples and redshift ranges, or, as discussed in Borisova et al. (2016), differing observational techniques, is beyond the scope of this work. However, we note that our simulations predict fairly ubiquitous LAHs in the presence of even moderate ionizing flux from the central black hole; in our simulated sample of quasars, only ∼15% had nebular emission below the observable threshold of 10^{-18} erg s^{-1} cm^{-2} arcsec^{-2} < 50 kpc from the halo (radially averaged). The predicted detection rate would thus appear to be in good agreement with the results of Borisova et al. (2016). Confirmation of a substantially lower detection rate would thus suggest that not all active quasars contain the ionizing photons necessary in our model to produce nebulae. This could be realized either if quasar emission were tightly beamed or if the quasar lifetime were short.

3.4.4. Surface Brightness Profiles

In Figure 9 we compare the full circularly averaged surface brightness profiles to the results of Cantalupo et al. (2014) and Borisova et al. (2016). Again, we used the "stars" model with $m_{\rm ion} = 1$ and a smoothing kernel with FWHM = 1 arcsec. Overall the agreement is very good, however, note that our profiles (solid lines) show the intrinsic SB values, whereas the observations (dashed lines) measure the SB after radiative transfer effects. This means our curves represent an upper limit on the measured SB levels due to the destruction of Lyα photons by dust. In particular, comparing the curve of Cantalupo et al. (2014) to our findings suggests an overall homogeneous escape fraction of $\gtrsim$10% as the slopes are comparable. The (averaged) SB profile of Borisova et al. (2016) is flatter in the inner region, which could be due to a higher dust attenuation in the central region and re-distribution to larger radii due to scatterings. This is not unreasonable as the central region possesses a larger optical depth, which makes photons originating there more vulnerable to destruction by

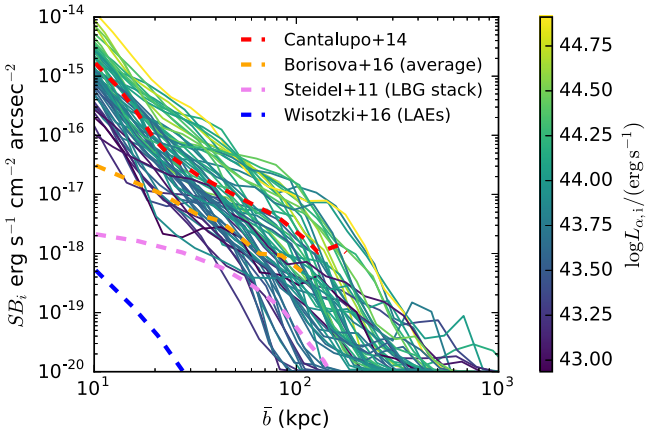

Figure 9. Circularly averaged intrinsic surface brightness profile for our sample of 60 nebulae between $10^{11.5}\,M_\odot$ and $10^{13.5}\,M_\odot$. Each solid curve represents the average $\mathrm{SB_i}$ profiles assembled from 10 randomly drawn viewing angles and is color coded according to the intrinsic Lyα luminosity. The dashed lines show the data from Cantalupo et al. (2014), Borisova et al. (2016), Steidel et al. (2011), and Wisotzki et al. (2016) (from top to bottom, extracted from Figure 5 of Borisova et al. 2016) as comparison. Note, however, that the data show the measured SB values and not the intrinsic ones (see Section 3.4 for a discussion).

dust and more likely to diffuse significantly in space before escape. We do in fact find this in the full radiative transfer simulations in Section 3.2 (comparing the intrinsic and post-processed SB profiles in Figure 3).

4. Conclusions

Several LAHs have recently been detected with unusually large extents ($\gtrsim$300 kpc) and observed Lyα luminosities ($\gtrsim 10^{44}$ erg s^{-1}) (Cantalupo et al. 2014; Hennawi et al. 2015). It has been speculated that this suggests the presence of substantial amounts of cold gas in cool clumps at densities that are not resolved by modern hydrodynamical simulations.

Using the publicly available data of the `Illustris` simulation (Vogelsberger et al. 2014; Nelson et al. 2015) we modeled the Lyα emission emerging from large halos ($M > 10^{11.5}\,M_\odot$) at $z \sim 2$. We considered two simple models: an AGN as source of ionizing photons, and ionization due to stars. We found for a single halo where we performed full Lyα radiative transfer that (i) with a moderately strong ionization source the halo showed intrinsic Lyα luminosities and extents comparable to observational data; (ii) additional clumping does not seem necessary to explain the first order properties of the observed giant LAHs, and (iii) due to the low optical depth of some routes, escaping Lyα photons often do not scatter, leading to a single peaked Lyα profile in both models. While the difference in the SB profiles cannot be used to distinguish between the models, the Lyα spectra are sensitive to sub-resolution properties such as the kinematics of the ISM and, thus, the question of whether or not the Lyα spectrum contains information about the main ionization source is still outstanding. In particular, changing the ionization state in the maximally ionized regions leads to a much greater optical depth at line center and thus an emergent double peak, as opposed to the single peaked profiles in our fiducial models. This difficulty might be the reason for the difference between observed spectra of Lyα nebulae, which are often double-peaked with an extended red- or blue-tail (e.g., Matsuda et al. 2006; Vanzella et al. 2017), and cosmological hydrodynamical simulations, which often predict a single peaked profile—as in this work (also see, e.g., Trebitsch et al. (2016)).

In order to put our fiducial halo into a wider context, we computed the intrinsic Lyα SB maps of 45 halos in the mass range $11.5 < \log M/M_\odot < 13.5$ and found that the observed objects fall within the range of computed maximal projected extents and Lyα luminosities. Furthermore, we found that that neither the maximal extent nor the total projected area of LAHs correlates significantly with other halo properties such as the total (intrinsic) Lyα luminosity, which we attribute to the stochastic nature of the gas-morphology.

Varying the surface brightness cutoff used for characterizing the extent of the LAHs, we find that multiplying (dividing) this value by a factor of three can increase (decrease) the maximal extent by $\sim$50%. This means not only that the nature of the previously detected "giant" LAHs might not be that different to the smaller ones detected previously, but also that we expect to find more of these objects in the near future.

This conclusion—i.e., that "giant LAHs" do appear in modern hydrodynamical simulations—differs from Cantalupo et al. (2014), who performed a similar analysis on one $\sim 10^{12.5}\,M_\odot$ halo extracted from a hydrodynamical simulation and found that substantial extra small-scale gas clumping was necessary to match their observations. We think this is for two reasons: (i) although their simulation included supernovae feedback, it did not include AGN feedback, which leads to a non-negligible distribution of gas for halos in this mass range (see, e.g., Genel et al. 2014; van Daalen et al. 2014, for an illustration of this effect); (ii) as we show in Figure 5 there is significant scatter in Lyα extents—even for fixed luminosity and/or size. Thus, a single halo producing a Lyα SB morphology as computed by Cantalupo et al. (2014) is entirely possible, even within Illustris.

The authors thank the anonymous referee for the constructive comments that significantly improved the manuscript. We thank M. Dijkstra and Ll. Mas-Ribas for a critical read of the draft. M.G. thanks the Physics & Astronomy department of Johns Hopkins University for their kind hospitality. S.B. was supported by NASA through Einstein Postdoctoral Fellowship Award Number PF5-160133. This research made use of Astropy, a community-developed core Python package for Astronomy (Astropy Collaboration et al. 2013); matplotlib, a Python library for publication quality graphics (Hunter 2007); SciPy (Jones et al. 2001).

Appendix
Intrinsic SB Maps

Figure 10 shows the intrinsic (i.e., without radiative transfer effects and (dust) extinction) surface brightness maps. These surface brightness maps have been assembled as described in Section 3.4 using a smoothing kernel with FWHM = 1 arcsec and from the same direction as Figure 2. In addition, we show in Figure 10 the SB = 10^{-18} erg s^{-1} cm^{-2} arcsec^{-2} levels from of the full radiative transfer simulation (Section 3.2) also smoothed with the same kernel.

One can note that compared to Figure 2 the intrinsic SB maps are first brighter in the central region due to the effect of dust extinction. This effect has been discussed in Section 3.2 (see Figure 3). Second, the scattering enlarges and washes out the SB contours. However, the extent for SB $\gtrsim 10^{-18}$ erg s^{-1} cm^{-2} arcsec^{-2} is comparable.

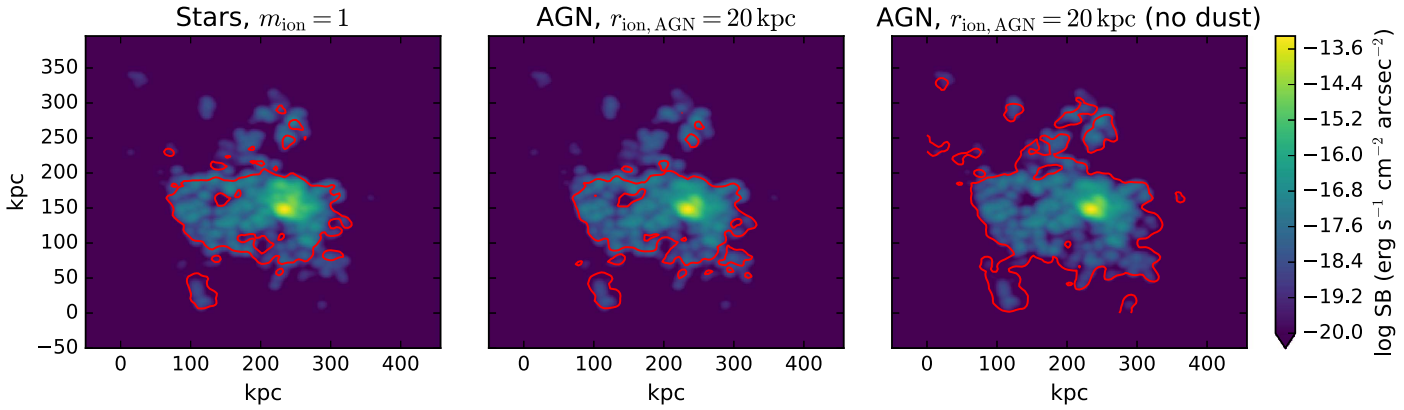

Figure 10. Intrinsic surface brightness maps for the fiducial models (see Section 2.2). The red lines denotes the SB $= 10^{-18}$ erg s^{-1} cm^{-2} arcsec^{-2} contours from of the full radiative transfer simulation (see Section 3.2 and Figure 2).

References

Ao, Y., Matsuda, Y., Beelen, A., et al. 2015, A&A, 581, A132
Astropy Collaboration, Robitaille, T. P., Tollerud, E. J., et al. 2013, A&A, 558, A33
Barnes, L. A., Garel, T., & Kacprzak, G. G. 2014, PASP, 126, 969
Battaia, F. A., Hennawi, J. F., Cantalupo, S., & Prochaska, J. X. 2016, arXiv:1604.02942
Borisova, E., Cantalupo, S., Lilly, S. J., et al. 2016, arXiv:1605.01422
Cantalupo, S., Arrigoni-Battaia, F., Prochaska, J. X., Hennawi, J. F., & Madau, P. 2014, Natur, 506, 63
Cantalupo, S., Porciani, C., & Lilly, S. J. 2008, ApJ, 672, 48
Cen, R., & Haiman, Z. 2000, ApJL, 542, L75
Cen, R., & Zheng, Z. 2013, ApJ, 775, 112
Dijkstra, M. 2014, PASA, 31, 26
Dijkstra, M., & Kramer, R. 2012, MNRAS, 424, 1672
Dijkstra, M., & Loeb, A. 2009, MNRAS, 400, 1109
Faucher-Giguère, C.-A., Kereš, D., Dijkstra, M., Hernquist, L., & Zaldarriaga, M. 2010, ApJ, 725, 633
Furlanetto, S. R., Schaye, J., Springel, V., & Hernquist, L. 2005, ApJ, 622, 7
Fynbo, J. U., Møller, P., & Warren, S. J. 1999, MNRAS, 305, 849
Genel, S., Vogelsberger, M., Springel, V., et al. 2014, MNRAS, 445, 175
Goerdt, T., Dekel, A., Sternberg, A., et al. 2010, MNRAS, 407, 613
Gould, A., & Weinberg, D. H. 1996, ApJ, 468, 462
Gronke, M., & Dijkstra, M. 2014, MNRAS, 444, 1095
Gronke, M., & Dijkstra, M. 2016, ApJ, 826, 14
Haiman, Z., & Rees, M. J. 2001, ApJ, 556, 87
Haiman, Z., Spaans, M., & Quataert, E. 2000, ApJL, 537, L5
Hayes, M. 2015, PASA, 32, e027
Hayes, M., Östlin, G., Duval, F., et al. 2014, ApJ, 782, 6
Hennawi, J. F., & Prochaska, J. X. 2013, ApJ, 766, 58
Hennawi, J. F., Prochaska, J. X., Cantalupo, S., & Arrigoni-Battaia, F. 2015, Sci, 348, 779
Herenz, E. C., Wisotzki, L., Roth, M., & Anders, F. 2015, A&A, 576, A115
Hui, L., & Gnedin, N. Y. 1997, MNRAS, 292, 27
Hunter, J. D. 2007, CSE, 9, 90
Jones, E., Oliphant, T., Peterson, P., et al. 2001, SciPy: Open Source Scientific Tools for Python
Laursen, P. 2010, PhD thesis, University of Copenhagen
Laursen, P., & Sommer-Larsen, J. 2007, ApJL, 657, L69
Laursen, P., Sommer-Larsen, J., & Andersen, A. C. 2009, ApJ, 704, 1640
Martin, D. C., Matuszewski, M., Morrissey, P., et al. 2015, Natur, 524, 192
Mas-Ribas, L., & Dijkstra, M. 2016, arXiv:1603.04840
Matsuda, Y., Yamada, T., Hayashino, T., et al. 2011, MNRAS, 410, 13
Matsuda, Y., Yamada, T., Hayashino, T., et al. 2012, MNRAS, 425, 878
Matsuda, Y., Yamada, T., Hayashino, T., Yamauchi, R., & Nakamura, Y. 2006, ApJL, 640, L123
Matthee, J., Sobral, D., Oteo, I., et al. 2016, MNRAS, 458, 449
Momose, R., Ouchi, M., Nakajima, K., et al. 2014, MNRAS, 442, 110
Nelson, D., Pillepich, A., Genel, S., et al. 2015, A&C, 13, 12
Osterbrock, D. E. 1989, Astrophysics of Gaseous Nebulae and Active Galactic Nuclei (Mill Valley, CA: University Science Books)
Pei, Y. C. 1992, ApJ, 395, 130
Price, D. J. 2012, JCoPh, 231, 759
Rahmati, A., Pawlik, A. H., Raičevic, M., & Schaye, J. 2013a, MNRAS, 430, 2427
Rahmati, A., Schaye, J., Pawlik, A. H., & Raičevic, M. 2013b, MNRAS, 431, 2261
Rauch, M., Haehnelt, M., Bunker, A., et al. 2008, ApJ, 681, 856
Reuland, M., van Breugel, W., Röttgering, H., et al. 2003, ApJ, 592, 755
Rosdahl, J., & Blaizot, J. 2011, arXiv:1112.4408
Springel, V. 2010, MNRAS, 401, 791
Steidel, C. C., Adelberger, K. L., Shapley, A. E., et al. 2000, ApJ, 532, 170
Steidel, C. C., Bogosavljević, M., Shapley, A. E., et al. 2011, ApJ, 736, 160
Steidel, C. C., Erb, D. K., Shapley, A. E., et al. 2010, ApJ, 717, 289
Trainor, R. F., & Steidel, C. C. 2012, ApJ, 752, 39
Trebitsch, M., Verhamme, A., Blaizot, J., & Rosdahl, J. 2016, arXiv:1604.02066
van Daalen, M. P., Schaye, J., McCarthy, I. G., Booth, C. M., & Dalla Vecchia, C. 2014, MNRAS, 440, 2997
Vanzella, E., Balestra, I., Gronke, M., et al. 2017, MNRAS, 465, 3803
Verhamme, A., Dubois, Y., Blaizot, J., et al. 2012, A&A, 546, A111
Villar-Martín, M., Sánchez, S. F., Humphrey, A., et al. 2007, MNRAS, 378, 416
Vogelsberger, M., Genel, S., Springel, V., et al. 2014, Natur, 509, 177
Wisotzki, L., Bacon, R., Blaizot, J., et al. 2016, A&A, 587, A98
Yusef-Zadeh, F., Morris, M., & White, R. L. 1984, ApJ, 278, 186
Zheng, Z., & Miralda-Éscude, J. 2002, ApJ, 578, 33